PANE Journal of Physics P. J. Phys. 02 (01), 033 (April 2026)

ENHANCED PHOTOCATALYTIC ACTIVITY OF MOF-DERIVED ZnO NANOPARTICLES FOR DYE DEGRADATION

Salam Jogita Chanu[1], L. Anju Chanu [1], and K. Nomita Devi[1*]

[1]*Department of Physics, Manipur University, Canchipur, Imphal 795003, India*

[*]Corresponding Author: kongkhamn@gmail.com

(Received 8 September 2025; revised 4 December 2025; accepted 5 December 2025; published 6 April 2026)

Abstract: In this study, the photocatalytic performance of Metal-Organic Framework (MOF) derived ZnO has been shown to be more efficient than the pure ZnO for Malachite Green (MG) dye degradation, a commonly used organic dye having considerable environmental influence. ZnO in pure form was prepared by chemical coprecipitation method and MOF-derived ZnO was prepared by self-assembly process. X-ray diffraction (XRD), energy dispersive X-ray spectroscopy (EDX), Field emission scanning electron microscope (FESEM), Fourier-transform infrared spectroscopy (FTIR), and UV-visible spectroscopy (UV-vis) were utilized to characterize the materials. XRD established that the two materials crystallize in the hexagonal wurtzite form, and FESEM established that pure ZnO was made up of both spherical and spindle-like particles, and MOF-derived ZnO consisted of mostly spherical particles. The UV-visible absorption spectra showed that both samples had bandgap energies of 3.32 eV. The photocatalytic performance (under UV light irradiation) of MOF-derived ZnO was excellent, as it was able to degrade MG dye by 98% in 3 hours. Such enhancement may be ascribed to the increased effective surface area and increased porosity of the MOF-derived structure which allows more effective photocatalysis.

Keywords: Metal-Organic Framework (MOF), Malachite Green, photocatalytic activity

PACS: 78.67.Bf, 61.46.-w, 78.67.-n, 78.40.-q

1 Introduction

Over the past century, the global demand of freshwater has increased owing to economic growth, population escalation and change in usage patterns. On the other hand, domestic, industrial, agricultural, and municipal activities, are exhausting the water resources increasing the water shortage and pollution, thereby making access to clean water one of the most pressing issues of modern society [1]. Among various pollutants, the wastewater of industrial productions like textiles, dye manufacturing, apparel, paper pulp, tanneries and printing is one of the major source of contamination [2]. Heavy metals (Zn, Ni, Cd, Cu, Pb, Hg, etc.), organic dyes ($e.g.$, methylene blue, Rhodamine B, malachite green), toxic chemicals, pesticides, herbicides, hydrocarbons, pharmaceuticals, $etc.$ are some of the harmful pollutants found in this industrial wastewater [3, 4]. Some of these chemicals are harmful, mutagenic, persistent in nature, and possess carcinogenic properties, creating a serious threat to both human health and environment [3, 5]. As per the World Health Organization (WHO), the textile industry accounts for approximately 17-20% of industrial wastewater pollution worldwide [6]. In the dyeing process, dyes are released into wastewater by 10-15%, which further degrades the quality of water [1, 6]. It is thus of much essence to manage the dye waste effectively before it is released to the environment to avoid the environmental pollution caused by the decomposition of dyes into forms that are non-toxic to the environment, reduction of contamination in the major water bodies, and effective elimination of the dyes in the aquatic environments.

The removal of dyes in wastewater has been done by applying various methods such as chemical precipitation, solvent extraction, coagulation-flocculation, biological treatments, and membrane filtration. Nevertheless, these

methods only transfer pollutants into sludge rather than completely eliminating them [4, 6]. To overcome these challenges, it is also requisite to have innovative, cost-effective, sustainable and energy efficient water purification process that can effectively remove contaminants with minimizing energy consumption and chemical usage [1, 7]. Advanced oxidation processes (AOPs) is an effective method of oxidizing and mineralizing diverse organic pollutants, which rely on highly reactive and strongly oxidizing radicals [7]. The high levels of efficacy in decontaminating pollutants to form less harmful byproducts and the high rates of degradation, as well as non-selective oxidation have made AOPs highly recognizable in wastewater treatment [4]. Semiconductor photocatalysis is one of the many AOPs that are highly effective in degrading toxic metal ions and organic pollutants [1, 2].

Photocatalysis, which is a process in which a semiconducting material produces electron-hole pairs in the presence of light of suitable wavelength. These charge carriers form reactive oxygen species (ROS), including superoxide anions ($O_2{\cdot}^-$) and hydroxyl radicals ($\cdot$OH), when in contact with water and oxygen and have strong oxidizing capabilities [4, 8]. These ROS are effective in the degradation of organic pollutants into harmless byproducts [5, 7, 9–11]. Photocatalysis is a renewable and environmentally friendly technology, therefore, it can be used to effectively degrade persistent hazardous contaminants with the use of sunlight [5, 12]. Additionally, it operates at room temperature, which not only makes the elimination for the need of high energy input but ensures that the pollutants are effectively degraded [2, 13]. Different metal oxide semiconductors, which are TiO_2, $ZnO, Bi_2O_3, Fe_2O_4, WO_3, Cu_2O, SnO_2$, etc., are highly active photocatalytic materials that facilitate the mineralization of organic pollutants [1, 2, 14–16]. Among the various metal-oxide semiconductors, ZnO and TiO_2 are most prospective materials used in degrading organic pollutants because of their high chemical robustness, non-toxicity, and strong oxidative potential [1, 15, 17–19]. Nevertheless, TiO_2 has low quantum efficiency and a small surface area when compared to ZnO, which is emerging to be a superior alternative as it has greater surface area, better quantum yield, and increased photoluminescence [16, 20, 21].

Moreover, Metal-Organic Frameworks (MOFs) have become a focal point of research due to their exceptionally large surface areas as well as highly tunable structures [8]. By self-assembly of metal ions and multidentate linkers, these three-dimensional and highly porous organic-inorganic frameworks are formed. They are highly versatile with regards to chemical and structural properties due to their large surface area, substantial pore volume, and tunable composition. The porosity of the MOFs is inherent in ion storage and transport [21, 22]. They can be integrated with metal oxides, which opens the potential for energy storage, catalysis, and remediation of the environment [8, 22]. Pure ZnO and MOF-derived ZnO have been prepared in this study through chemical co-precipitation method and self-assembly method, respectively. The resulting photocatalyst were characterized by X-ray diffraction (XRD), Field emission scanning electron microscope (FESEM), energy-dispersive X-ray spectroscopy (EDX), Fourier-transform infrared spectroscopy (FTIR), and UV-visible spectroscopy (UV-vis). Their photocatalytic performance was subsequently evaluated for the degradation of Malachite Green dye.

2 Materials and Methods

2.1 Materials Required

In this study, analytical grade Zinc Nitrate Hexahydrate ($Zn(NO_3)_2 \cdot 6H_2O$, Sigma-Aldrich), 2-Methylimidazole ($C_6H_6N_2$, Sigma-Aldrich), Sodium Hydroxide (NaOH, Merck) and Malachite Green ($C_{23}H_{25}ClN_2$, Hi-Media) were used as reagent without further treatment. Distilled water (DI) is used as a solvent for the entire experiment.

2.2 Synthesis of pure ZnO

Pure ZnO nanoparticles were synthesized by the facile chemical co-precipitation method. Initially, 0.1 M of $Zn(NO_3)_2 \cdot 6H_2O$ was dispersed in 200 mL of deionised (DI) water and magnetically stirred for 30 min at room temperature (27°C). Similarly, 0.5 M NaOH solution in 300 ml of DI water was prepared with continuous stirring for 30 min. The NaOH solution was then introduced gradually into the $Zn(NO_3)_2 \cdot 6H_2O$ solution until the pH reached 12 and kept stirring for another 2 hours. The resulting precipitate was washed numerous times with DI water, dried in an oven at 80°C for about 2 days until it was completely dry and ground to obtain ZnO powder.

2.3 Synthesis of MOF-derived ZnO

MOF-derived ZnO nanoparticles were synthesized via a self-assembly process. The starting materials, $Zn(NO_3)_2 \cdot 6H_2O$ and 2-Methylimidazole, were used in a 1:4 molar ratio. 0.594g of $Zn(NO_3)_2 \cdot 6H_2O$ was dissolved in

50mL of DI water and magnetically agitated at 300 rpm at room temperature for 30min. Separately, 0.656g of 2-Methylimidazole was dissolved in 50ml of DI water. The $Zn(NO_3)_2 \cdot 6H_2O$ solution was then introduced to the 2-Methylimidazole solution, and the mixture was continuously stirred overnight on a hot plate. The precipitate so formed was washed and collected by centrifugation, dried in an oven at 80°C and then finely ground into powder. Finally, the finely powdered sample was subjected to calcination at 500°C for 6 hours to obtain MOF-derived ZnO.

2.4 Characterization

Powder X-Ray diffraction (XRD) was used to determine the phase composition of pure ZnO and MOF-derived ZnO with the X'Pert Pro PANalytical diffractometer equipped with Cu Kα radiation. The Field emission scanning electron microscopy (FESEM) was used alongside EDX spectroscopy to analyze its morphological characteristics, as well as its elemental constitution. The UV-visible spectra of the materials were taken on a Perkin Elmer Lambda-365 UV-Vis Spectrophotometer. The functional group and the chemical bond of the particles were determined by the Perkin Elmer FTIR Spectrum 2 IR spectrometer.

2.5 Photocatalytic activity test

Photodegradation experiment was conducted by using Malachite Green dye as the model pollutant and irradiated by UV-C light from an 8W mercury lamp. In a typical photocatalytic procedure, the catalyst was dispersed into the dye solution and subjected to ultrasonication. To achieve a state of adsorption-desorption equilibrium, the catalyst-loaded dye suspension was stirred in the dark for 1 hour and thereafter it was irradiated with the light source. Aliquots of the irradiated solution were then taken at regular interval of time and their absorbance was recorded with the help Ocean Optics HR 4000 UV-Vis Spectrophotometer. The photocatalytic efficiency of the synthesized samples was assessed based on percentage degradation, calculated using the following Eq. (1) [23].

$$\% \text{ of Degradation} = \frac{C_0 - C}{C_0} \times 100 = \frac{A_0 - A}{A_0} \times 100 \tag{1}$$

where C_0 represents the initial dye concentration, C represents the concentration after irradiation, A_0 denotes the initial absorbance, and A denotes the absorbance of the solution measured after irradiation.

3 Results and Discussion

3.1 Structural characterization

Fig. 1(a), 1(b) and 1(c) illustrate the XRD patterns of pure ZnO nanoparticles, pure MOF and MOF-derived ZnO nanoparticles, respectively. The diffracted patterns in Fig. 1(a) and 1(c) exhibit characteristic Bragg reflections corresponding to the crystallographic planes: (202), (004), (201), (112), (200), (103), (110), (102), (101), (002), and (100), along with their corresponding 2θ values. The peaks of the diffraction confirm the existence of hexagonal wurtzite phase of ZnO (ICSD card number: 01-075-0576). Scherrer's formula (Eq. (2)) was used to estimate the crystallite size, which was calculated to be 18 nm and 24 nm for pure ZnO and MOF-derived ZnO respectively.

$$g = \frac{k\lambda}{\beta \cos\theta} \tag{2}$$

where g denotes the crystallite size (nm), λ is the wavelength of the X-ray (nm), k is the shape factor or Scherrer constant (0.9), θ is the Bragg angle (radians), and β is the full width at half maximum of the diffraction peaks (radians) [24].

The XRD pattern of the synthesized MOF, as shown in Fig. 1(b), exhibits distinct diffraction peaks corresponding to the characteristic planes of its crystalline framework, confirming its successful formation [25].

The measured positions and intensities of the observed peaks are comparable with those of the MOF structures which crystallized in the hexagonal phase and is highly similar to the reference pattern indexed in the JCPDS card no. 00-062-1030, thus confirming the high purity and crystallinity of the phase in the obtained material [26–29].

The controlled growing environment of the MOF precursor, which facilitates uniform nucleation and growth of the crystal is the reason behind the slightly larger size of the MOF-derived ZnO [22]. The intense, sharp peaks suggest high levels of crystallinity, which facilitates rapid electron transport and slow down recombination and contribute to the high photocatalytic activity of MOF-derived ZnO in MG dye degradation [30].

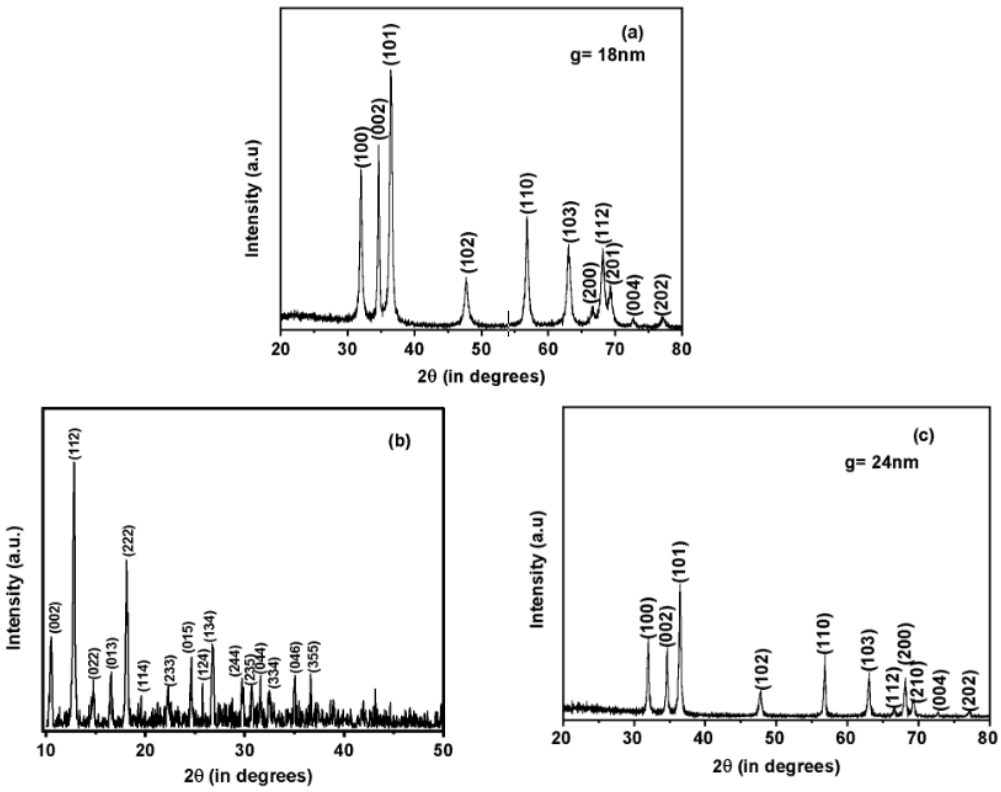

Figure 1: XRD patterns of the synthesized samples (a) pure ZnO, (b) ZIF-8 MOF, and (c) MOF-derived ZnO.

3.2 Morphological and compositional analysis

FESEM was used to study the surface morphology of the synthesized samples. As shown in Fig. 2(a), the pure ZnO nanoparticles exhibit a mixture of spherical and spindle-like structures. In contrast, Fig. 2(c) reveals that the MOF-derived ZnO crystals predominantly exhibit an agglomerated spherical morphology. The corresponding particle size distribution histograms, presented in Fig. 2(b) and 2(d), were fitted using a log-normal distribution function [31]:

$$f_d = \frac{1}{d\sigma\sqrt{2\pi}} \exp[\frac{(\ln d - \mu)^2}{2\sigma^2}], \tag{3}$$

where d is the particle diameter, σ is the standard deviation of $\ln d$, μ is the mean of $\ln d$.

Average particle size was estimated from the fitted parameters according to the standard expression for a log-normally distributed variable [32]:

$$d_{avg} = \exp[\frac{\mu + \sigma^2}{2}] \tag{4}$$

Using this relation, the average particle sizes of the pure ZnO and MOF-derived ZnO were estimated to be 175 nm and 92 nm, respectively. The significantly smaller and more uniform particle size of the MOF-derived sample highlights the structural templating of the MOF precursor, which promotes the formation of finer ZnO nanoparticles with enhanced surface area and improved physiochemical properties, including photocatalytic performance.

Fig. 3(a) and 3(b), respectively display the elemental composition of pure ZnO and MOF-derived ZnO. The presence of emission peaks corresponding to Zn and O atoms only are observed in the EDX spectra, with no additional peaks, which confirms the sample purity.

3.3 UV-Vis Absorption Spectroscopy

Fig. 4(a) and 4(b) depict the UV-Vis absorption results of pure ZnO and MOF-derived ZnO nanoparticles, respectively, with 367 nm and 373 nm as the absorption peaks. The optical band gap (Eg) was also estimated using the

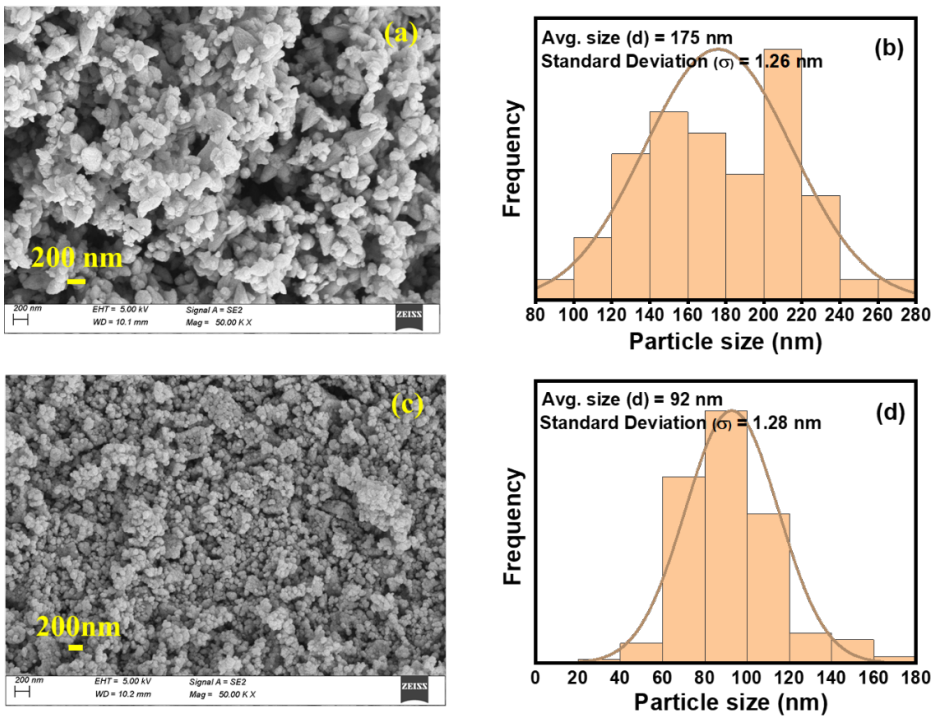

Figure 2: Surface morphology observed by FESEM and particle size distribution histograms of (a) FESEM image of pure ZnO and (b) particle size distribution of pure ZnO fitted with a log-normal distribution (c) FESEM image of MOF-derived ZnO (d) particle size distribution of MOF-derived ZnO fitted with a log-normal distribution.

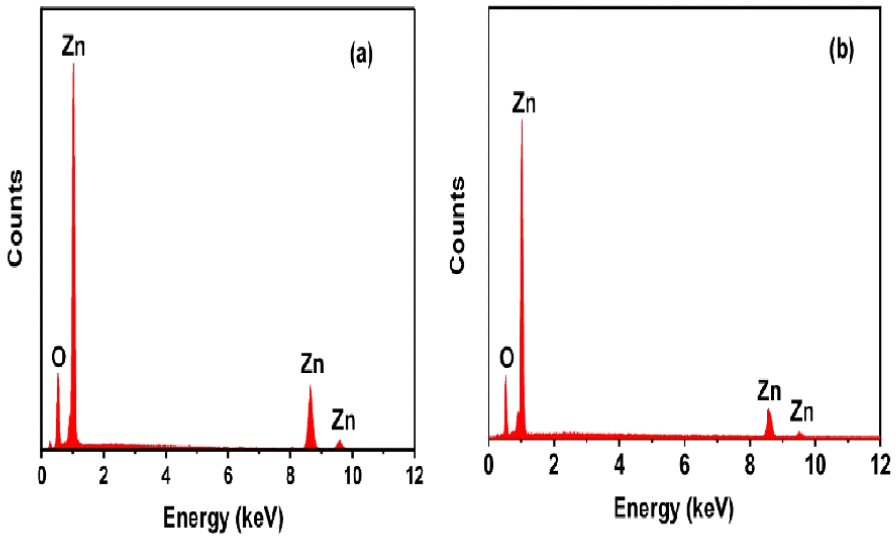

Figure 3: EDX spectra of the synthesized samples (a) pure ZnO and (b) MOF-derived ZnO.

following relation [33]:

$$E_g = \frac{hc}{\lambda} \tag{5}$$

where c represents the speed of light, h denotes Planck's constant, and λ corresponds to the wavelength of the respective absorption peak.

The band gap energy of pure ZnO and MOF-derived ZnO was determined to be 3.32 eV.

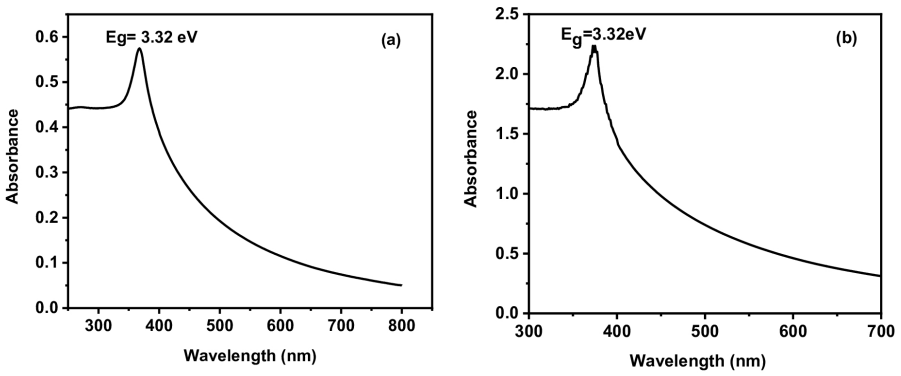

Figure 4: UV-vis absorption spectra of the synthesized samples (a) pure ZnO and (b) MOF-derived ZnO.

3.4 Fourier Transform Infrared (FTIR) Spectra

The Fourier transform infrared (FTIR) spectrum of pure ZnO and MOF-derived ZnO, are presented in Fig. 5(a) and 5(b), respectively. For pure ZnO, a prominent absorption band corresponding to the Zn–O stretching vibration is observed at 410 cm^{-1}. In the case of MOF-derived ZnO, this band is slightly shifted to 416 cm^{-1}, which may be attributed to lattice distortions, altered crystallite size, or structural modifications induced during the MOF-to-ZnO transformation [34].

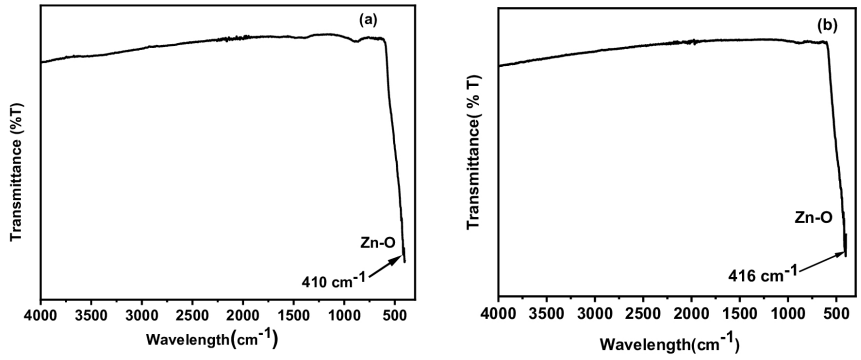

Figure 5: FTIR spectra of synthesized samples (a) pure ZnO and (b) MOF-derived ZnO.

3.5 Evaluation of the photocatalytic activity on MG dye

Fig. 6(a) and 6(b) show the photocatalytic degradation curves of pure ZnO and MOF-derived ZnO upon UV light irradiation. Pure ZnO achieves 76% degradation of MG under 3 hours of irradiation, whereas MOF-derived ZnO reaches 98% degradation in just 3 hours. This enhanced photocatalytic performance is ascribed to the MOF-derived architecture, which provides increased surface area and porosity, thereby facilitating more efficient dye degradation [22].

Kinetics of the photocatalytic reaction was studied by applying the Langmuir-Hinshelwood model, which reveals that the reaction followed the pseudo-first-order kinetics. This relationship is expressed as Eq. (4) [35]

$$\ln\frac{C_0}{C} = kt \tag{6}$$

where C_0 and C denote the initial and final concentration of dye prior to and following irradiation, respectively, k is the pseudo first order rate constant, t is the irradiation time. Table 1 indicates the values of the rate constants

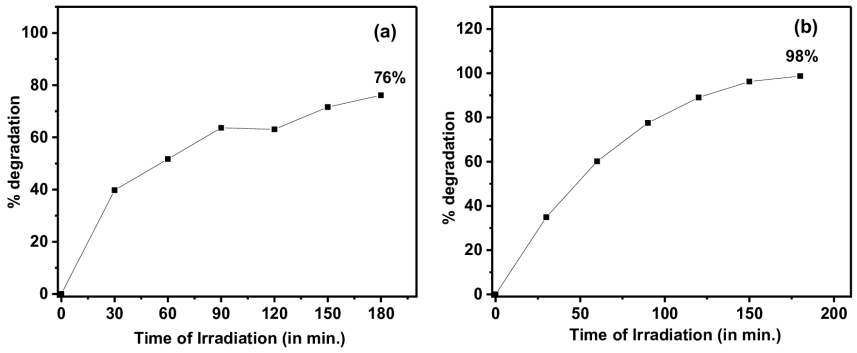

Figure 6: Photocatalytic degradation curves for (a) pure ZnO and (b) MOF-derived ZnO.

calculated. The two distinct linear areas in the kinetic plot may be explained as follows:

$$\text{Organic Dye} \rightarrow \text{Adsorption} \xrightarrow{k_1} \text{Intermediate Product} \xrightarrow{k_2} \text{Colourless Product}$$

Photocatalyst	**Rate constant,** k_1 **(**10^{-2} **per min)**	**Rate constant,** k_2 **(**10^{-2} **per min)**
MOF – derived ZnO	1.7	3.2
Pure ZnO	1.2	0.8

Table 1: Reaction rate constants calculated for the synthesized samples.

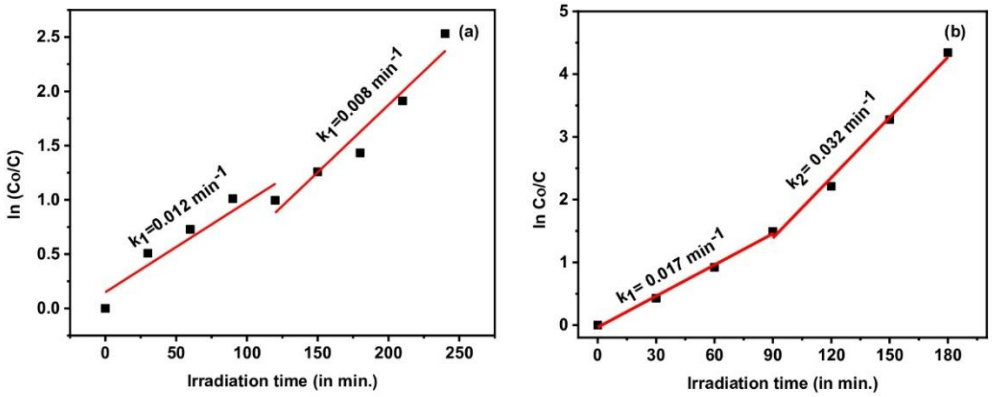

Figure 7: Plot of $\ln(C_0/C)$ vs. irradiation time for (a) pure ZnO and (b) MOF-derived ZnO.

4 Conclusions

In conclusion, pure ZnO nanoparticles and MOF-derived ZnO nanoparticles were prepared using chemical co-precipitation method and self-assembly technique, respectively. XRD analysis confirmed that both samples were in the hexagonal wurtzite structure. FESEM micrographs proves that pure ZnO was a composite of both spherical and spindle-like particles, but the MOF-derived ZnO was more likely to have the morphology of a sphere. The use of energy-dispersive X-ray (EDX) spectroscopy technique established that the samples only contained zinc and oxygen. The UV-visible absorption spectra were used to estimate the optical bandgap energies, which means that both samples can be applied in the UV region. The photocatalytic efficiency of MOF-derived ZnO was found to be better degrading 98% of MG dye under the UV light in 3 hours. These findings highlight the possibility of MOF-derived ZnO to be an efficient photocatalyst in eliminating organic pollutants.

References

[1] N. Nayak, S. Singha, J. P. Maity, P. P. Rath, T. Sahoo, and T. R. Sahoo, Journal of Materials Science: Materials in Electronics **35**, 310 (2024).

[2] R. Sarathi, L. Renuga Devi, N. L. Sheeba, E. Selva Esakki, and S. Meenakshi Sundar, Journal of Chemical Reviews **5**, 15 (2023).

[3] D. Sahoo, S. Tyagi, S. Agarwal, J. Shakya, N. Ali, W. J. Yoo, and B. Kaviraj, Langmuir **39**, 7109 (2023).

[4] P. Singh, B. Mohan, V. Madaan, R. Ranga, P. Kumari, S. Kumar, V. Bhankar, P. Kumar, and K. Kumar, Environmental Science and Pollution Research **29**, 69294 (2022).

[5] S. Meena, D. Vaya, and B. K. Das, Bulletin of Materials Science **39**, 1735 (2016).

[6] M. O. Chijioke-Okere, N. J. Okorocha, B. N. Anukam, and E. E. Oguzie, International Letters of Chemistry, Physics and Astronomy **81**, 18 (2019).

[7] T. Ahuja, U. Brighu, and K. Saxena, Journal of Water Process Engineering **53**, 103759 (2023).

[8] S. Chaudhari, A. Kularkar, S. Devi, and P. Nagababu, Journal of Physics and Chemistry of Solids **188**, 111929 (2024).

[9] A. M. Saad, M. R. Abukhadra, S. Abdel-Kader Ahmed, A. M. Elzanaty, A. H. Mady, M. A. Betiha, J.-J. Shim, and A. M. Rabie, Journal of Environmental Management **258**, 110043 (2020).

[10] W. S. Koe, J. W. Lee, W. C. Chong, Y. L. Pang, and L. C. Sim, Environmental Science and Pollution Research **27**, 2522 (2020).

[11] A. Balapure, J. Ray Dutta, and R. Ganesan, RSC Applied Interfaces **1**, 43 (2024).

[12] J. Kalita, L. Bharali, and S. S. Dhar, New J. Chem. **46**, 20182 (2022).

[13] S. N. Ahmed and W. Haider, Nanotechnology **29**, 342001 (2018).

[14] R. E. Adam, G. Pozina, M. Willander, and O. Nur, Photonics and Nanostructures - Fundamentals and Applications **32**, 11 (2018).

[15] R. Ullah and J. Dutta, Journal of Hazardous Materials **156**, 194 (2008).

[16] D. Dodoo-Arhin, T. Asiedu, B. Agyei-Tuffour, E. Nyankson, D. Obada, and J. Mwabora, Materials Today: Proceedings **38**, 809 (2021), 2020 International Symposium on Nanostructured and Advanced Materials.

[17] S. Kerli, M. Kavgacı, A. K. Soğuksu, and B. Avar, Brazilian Journal of Physics **52**, 22 (2021).

[18] N. Qutub, P. Singh, S. Sabir, S. Sagadevan, and W.-C. Oh, Scientific Reports **12**, 5759 (2022).

[19] Y. Wang, C. Hou, X. Lin, and H. Jiang, SN Applied Sciences **1**, 743 (2019).

[20] S. H. Ribut, C. A. Che Abdullah, M. Mustafa, M. Z. Mohd Yusoff, and S. N. Ahmad Azman, Materials Research Express **6**, 025016 (2018).

[21] S. Sheikhi, M. Aliannezhadi, and F. Shariatmadar Tehrani, European Physical Journal Plus **137**, 60 (2022).

[22] P. Abisha, J. C.G., and S. Sonia, Current Applied Physics **60**, 79 (2024).

[23] L. A. Chanu, K. J. Singh, and K. N. Devi, Integrated Ferroelectrics **204**, 90 (2020).

[24] L. Anju Chanu, W. Joychandra Singh, K. Jugeshwar Singh, and K. Nomita Devi, Results in Physics **12**, 1230 (2019).

[25] Y. Jing, J. Wang, B. Yu, J. Lun, Y. Cheng, B. Xiong, Q. Lei, Y. Yang, L. Chen, and M. Zhao, RSC Adv. **7**, 42030 (2017).

[26] Y. Sun, H. Zhang, Y. Lv, S. An, and R. Wang, RSC Adv. **14**, 17498 (2024).

[27] J. Chen, Y. Yang, S. Yu, Y. Zhang, J. Hou, N. Yu, and B. Fang, Nanomaterials **13** (2023).

[28] I. Rabani, S. A. Patil, M. S. Tahir, F. Afzal, J.-W. Lee, H. Im, Y.-S. Seo, and N. K. Shrestha, Nanomaterials **13** (2023).

[29] K. Zhou, B. Mousavi, Z. Luo, S. Phatanasri, S. Chaemchuen, and F. Verpoort, J. Mater. Chem. A **5**, 952 (2017).

[30] Q. Wang and D. Astruc, Chemical Reviews **120**, 1438 (2020).

[31] S. K. Paswan, S. Kumari, M. Kar, A. Singh, H. Pathak, J. Borah, and L. Kumar, Journal of Physics and Chemistry of Solids **151**, 109928 (2021).

[32] M. Molaei, M. Abdollahi, A. M. Zardkhoshoui, and S. S. H. Davarani, Journal of Energy Storage **85**, 111079 (2024).

[33] L. A. Chanu, K. J. Singh, and K. N. Devi, AIP Conference Proceedings **2265**, 030052 (2020).

[34] C. Berthomieu and R. Hienerwadel, Photosynthesis Research **101**, 157 (2009).

[35] L. Anju Chanu, K. Jugeshwar Singh, and K. Nomita Devi, Materials Today: Proceedings **65**, 2865 (2022).